

Strong self-focusing in nematic liquid crystals

Erez Braun, Luc P. Faucheux, and Albert Libchaber*

Department of Physics, Princeton University, Princeton, New Jersey 08544-0708

(Received 1 October 1992)

We present an experimental study of strong self-focusing in nematic liquid crystals. In a planar geometry, a linear dependence of the focal power on the input intensity for 100- μm -thick samples turns into an exponential one when thicker samples are used. A transverse visualization of the beam structure is performed in a cylindrical geometry. We observe an undulation and a filamentary structure of the laser beam for large intensities. Also, multiple focal points appear along the beam axis in this configuration. Undulation and filamentation of the beam are also observed in a spherical geometry.

PACS number(s): 42.65.Jx, 42.70.Df

I. INTRODUCTION

Optical self-focusing stands among the many phenomena caused by a light-matter interaction. It occurs when light modifies a medium such that it creates an intensity-dependent focusing lens [1–7]. One can question the limit of such a nonlinear retroaction, where diffraction competes against focusing, the latter being a combination of the input intensity and the material response. The natural way to study this limit is to push the focusing term into a regime where nonlinear effects become appreciable. Due to the small value of the coefficient of optical nonlinearity in most materials, experiments were performed using high-power laser pulses [8], introducing an external time dependence. On the other hand, because of the large optical nonlinearity in nematic liquid crystals (due to the reorientation of the director field), a moderate continuous beam [9–11] can be used. Besides, what makes liquid crystals unique is their elastic response to alignment: the self-focusing effects depend upon the boundary conditions and geometry of the system.

We present an experimental study of self-focusing of a continuous laser beam in nematic liquid crystals. The simplest configuration consists of a flat sample, thin enough to be considered as a small perturbation to the incident laser beam (hereafter called the pump beam). Using a secondary laser beam (hereafter called the probe beam) to measure the focusing power of the sample, we then recover the usual linear dependence upon the pump-beam intensity [10,11]. This happens when the focal point is outside the sample. However, when this focal point moves inside the liquid crystal for thick samples, we observe a deviation from the linear dependence: the focal power increases exponentially with intensity. At high intensity, the probe beam breaks into filaments, rendering our measurement-technique useless.

This led us to adopt a quasi-semi-infinite cylindrical configuration, where we can look directly at the longitudinal evolution of the pump beam itself inside the liquid crystal. The laser beam is aligned along the axis of a long cylindrical sample with forced cooling along its surface, in order to avoid possible heating effects. At low intensity, the change in the position of the pump-beam focal

point is consistent with our results in the planar geometry. A striking result is the observation at high intensity of a steady spatial undulation of the beam inside the tube. The longitudinal characteristic length of this oscillation first decreases with intensity, reaches a minimum, and then increases. In the latter regime, we encounter another phenomenon: the beam develops an inner filamentary structure.

These observations suggest a possible separation of the focusing effect into two aspects, each with its own length scale: an outer one describing the beam undulation, and an inner one for the beam structure. The undulation and the inner filamentary structure can be recovered in a simple mathematical model where, as opposed to the classical theory based on a local expansion of the optical index, the elastic response of the medium plays a crucial role [12]. In particular, the elastic term appears to be the restoring force when the beam undulates. Based on this elastic effect and on the birefringing nature of the nematic liquid crystal, we present a simple geometric model for the beam undulation.

For larger intensities, the beam exhibits a random dynamic behavior. Understanding this dynamic behavior will require a time-dependent model.

The paper is organized as follows: We present in Sec. II the experimental results for the planar geometry and discuss the exponential increase of the focal power in thick samples. In Sec. III we describe the observation of the beam in the cylindrical geometry at low intensity. We discuss in Sec. IV the beam undulation, and present the filamentary structure. Similar observations in a spherical geometry are described in Sec. V. We summarize the results in Sec. VI. The Fréedericksz transition, as well as measurements of the intensity threshold, is presented in the Appendix.

II. SELF-FOCUSING IN PLANAR GEOMETRY

In this section, we restrict ourselves to self-focusing in a planar geometry. We introduce the Fréedericksz transition and the light-nematic interaction in thin samples. We then turn to thick samples where we observe a sharp increase of the focusing effect upon intensity.

A. Experimental setup

We studied the liquid crystals *N*-(4'-methoxybenzylidene)-4-(*n*-butyl)aniline (MBBA), 4-cyano-4'-*N*-hexylbiphenyl (6CB), and E209 in the nematic phase [13]. MBBA and 6CB are well-known pure materials, while E209 is a less standard commercial compound (BDH, Ltd., Poole, England). The temperature ranges for the nematic phase are, respectively, from 16 to 46°C, from 15 to 29°C, and from -50 to 111°C. The experiments are performed at a temperature of 22.0 ± 0.5 °C.

Flat samples are prepared in the following way: a cell is composed of two glass plates separated by mylar spacers and sealed with Torr-Seal [14]. The sample thickness varied from 100 μm to 2000 μm . The two glass plates are coated with a silane surfactant [15] to achieve homeotropic alignment of the director (i.e., perpendicular to the surface). The liquid crystal is then injected inside the cell. We check the director alignment by the conoscopy technique [16].

The experimental setup is shown in Fig. 1. A linearly polarized Argon laser beam (the pump beam), in the TEM₀₀ Gaussian mode, is applied perpendicular to a sample that sits on the stage of an inverted microscope. Our control parameter is the intensity of the pump beam, which we adjust with a 50-mm converging lens placed above the sample. Given the total laser power and the beam spot size at the bottom of the sample (our plane of reference, which is easily identified with the microscope), we deduce the beam intensity. This spot size is typically around 50 μm . A second, weak He-Ne laser beam (the probe beam) of 3 mW power is combined with the pump via a cube beam splitter. The two beams are aligned with an accuracy of a few microns and have the same linear polarization. They enter directly into the microscope 4 \times objective. The measurement itself is done in the following way: The pump beam, which excites the medium, is strongly attenuated by a filter after the sample. We measure with the inverted microscope the changes in the position of the waist of the probe beam as a function of the

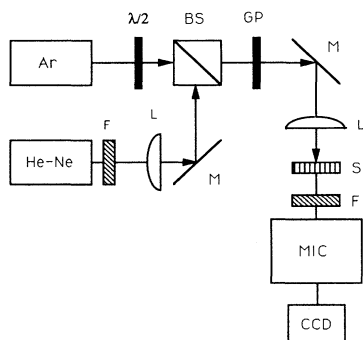


FIG. 1. Setup for the measurement of the onset of director deformation and self-focusing in planar geometry: Ar, argon laser (pump beam); He-Ne, helium neon laser (probe beam); $\lambda/2$, half wave plate; BS, cube beam splitter; GP, Glan polarizer; M, mirror; L, converging lens; S, sample; F, red color filter; MIC, microscope; CCD, charge-coupled-device camera.

pump intensity. The distance between this beam waist and the bottom plate of the sample can be measured with an accuracy of 10 μm . The bigger this distance, the more sensitive is our measurement. In order to achieve the maximum distance within the range of the microscope, we put a long focal-distance lens on the path of the probe beam before combining it with the pump one. This allows us to adjust the sensitivity of the measurement without affecting the control parameter. We also require the probe spot size at the sample to be close to the one of the pump beam, so that the two beams explore the same region of the nematic liquid crystal. Under these conditions, the results obtained are insensitive to the specific optical setup. By using geometrical optics, the position change of the beam waist can be translated into an absolute focal length of an equivalent thin lens. Let us turn now to the onset of the director deformation.

B. Fréedericksz transition

When an electric field is applied at optical frequency, the nematic director tends to align along its direction for the liquid crystals used in the experiment. Due to the boundaries which impose the initial director alignment, an elastic restoring torque is also present. The balance between these two defines the onset of the Fréedericksz transition at a threshold intensity I_{Fr} [16]. The order parameter of this transition is the director deformation angle. We present in the Appendix measurements of I_{Fr} and of the time scales associated with this transition for the 100- μm samples. We also give there an estimate of the director penetration length. We present in the table the experimental results for the different liquid crystals.

C. Self-focusing

Above the Fréedericksz transition, the director deformation modifies the local refractive index, which in turn affects the propagation of the beam through the sample. Since a higher intensity in the middle of the beam produces a higher refractive index, the beam focuses as it propagates through. However, this effect is appreciable only when the index profile is powerful enough to overcome diffraction. This leads to a threshold for self-focusing I_{SF} , which is larger than the threshold for the nematic director deformation I_{Fr} .

In the focusing regime, the position change of the probe beam waist is measured by the method described above. The results are shown in Fig. 2 for different samples. We can clearly identify two distinct behaviors: Thin samples (100 μm) exhibit a linear dependence of the focal power on the pump intensity, while thicker ones (~ 1000 μm) display an exponential increase. We show below that these data can be encompassed in one universal curve.

We follow here a standard derivation for the propagation equation of light inside a focusing medium [5,17]. We assume a local Kerr expansion for the refractive index: $n = n_o + n_2 \tilde{I}$, where n_o is the ordinary refractive index and n_2 is the nonlinear coefficient. \tilde{I} is the increase in the pump-beam intensity above I_{Fr} . We consider the propagation of a Gaussian beam, with a spot size a , an in-

tensity I , and an initial planar wave front across a small thickness δz of nematic. If r is the transverse direction, we expand the optical index $n(r) = n_0 + n_2(I - I_{\text{Fr}})e^{-2r^2/a^2}$ around $r=0$, to get for the change of the wave-front curvature

$$\delta C = \frac{\partial^2 [n(r)\delta z]}{\partial r^2} = 4n_2(I - I_{\text{Fr}})a^{-2}\delta z. \quad (1)$$

This defines a characteristic length scale associated with self-focusing: $z_f^{-2} = \delta C / \delta z = 4n_2(I - I_{\text{Fr}})a^{-2}$.

A sample of thickness d is defined as thin when $d \ll z_f$. This leads to a linear dependence of the inverse focal length on the pump intensity, as has already been observed [17–20]. In this limit we assume a constant spot size a across the sample, and we integrate Eq. (1) along the direction of propagation to get $C = 4n_2(I - I_{\text{Fr}})a^{-2}d$. C is the inverse focal length of a thin converging lens equivalent to the sample. Due to diffraction, the real curvature of the wave front after the sample is $f^{-1} = C - 1/ka^2$, where k is the wave vector. The

threshold for self-focusing I_{SF} corresponds to $f^{-1} = 0$, or

$$I_{\text{SF}} = I_{\text{Fr}} + [4n_2dk]^{-1}. \quad (2)$$

We then rewrite f^{-1} as

$$f^{-1} = 4n_2(I - I_{\text{SF}})da^{-2}. \quad (3)$$

Fitting the measurements of Fig. 2 for thin samples with a straight line corresponding to Eq. (3), we obtain n_2 and I_{SF} . The values are reported in Table I. The value of I_{Fr} is then obtained from Eq. (2), and is consistent with the measurements described in the Appendix and reported in the table. The values of n_2 are somewhat lower than those observed previously [9]. Note, however, that we work in a different intensity regime than in previous publications.

As opposed to thin samples, thicker ones exhibit a sharp increase of the focal power as a function of intensity, best fitted by an exponential. When the thickness is of the order of the focusing scale, $d \sim z_f$, let us show that the focal point moves into the sample. From Eq. (1), C scales as Ia^{-2} and as the total beam power Ia^2 is conserved, it scales as a^{-4} . Thus one can neglect $1/ka^2$ and write $f^{-1} \sim C$. As C is equal to d/z_f^2 , one gets $d/f \sim 1$, and the focal point moves into the nematic region.

We try next to encompass all the data from Fig. 2 into a universal curve. The obvious way to do this is to plot d/f versus the dimensionless curvature acquired by the wave front across the sample: $4n_2(I - I_{\text{SF}})(d/a)^2$. Unfortunately, this does not lead to a universal dependence. We encounter here the complexity of the light-nematic interaction: the local Kerr expansion that we assumed is a good approximation as long as $d \ll z_f$. The change in the dependence of the focusing power upon intensity when $d \sim z_f$ clearly shows the limits of this assumption. If we keep the functional form for the expansion of the refractive index, we have to allow n_2 to be dependent upon the geometry, size, and boundary conditions of the specific sample: the nematic liquid crystal is not a Kerr medium and n_2 cannot be considered as a material constant.

On empirical grounds, we find that the universal control parameter is $R = 4n_2(I - I_{\text{SF}})(d/a)^2(d_e/d)$. The

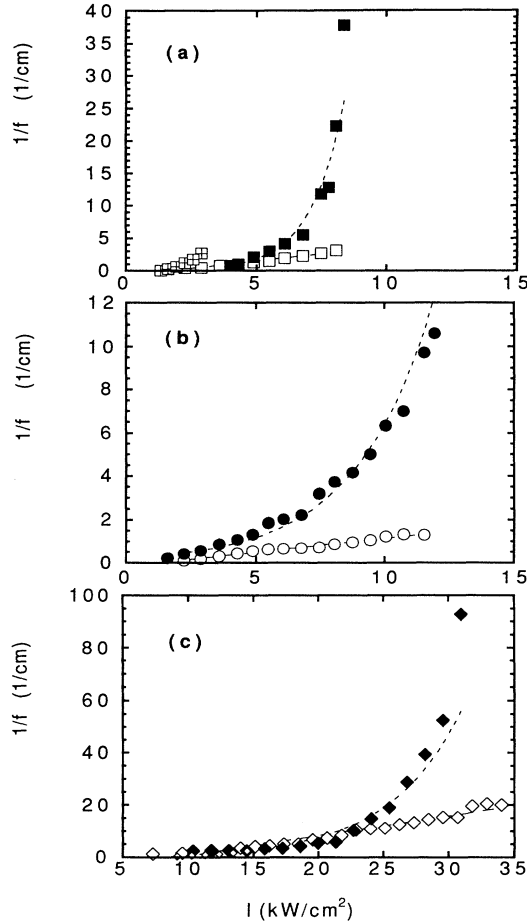


FIG. 2. Inverse focal length as a function of the pump intensity for plane samples of (a) MBBA: $d = 100 \mu\text{m}$ (empty squares), $1000 \mu\text{m}$ (filled squares), and $2000 \mu\text{m}$ (crossed squares). (b) 6CB: $100 \mu\text{m}$ (empty circles) and $700 \mu\text{m}$ (filled circles). (c) E209: $100 \mu\text{m}$ (empty diamonds) and $940 \mu\text{m}$ (filled diamonds). The dashed lines are best fits to the data; linear fits for thin samples and exponential fits for thick ones.

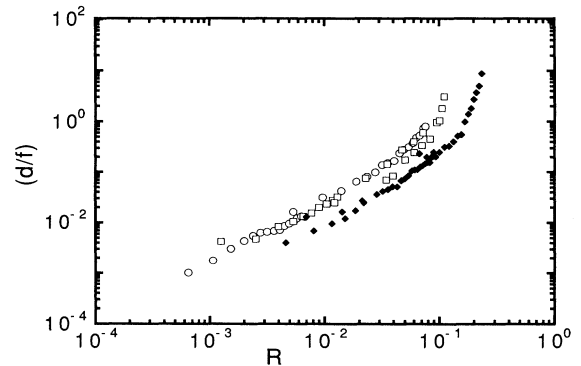


FIG. 3. Dimensionless focal powder d/f vs the control parameter R (see text for the definition), for MBBA (empty squares), 6CB (empty circles), and E209 (filled diamonds). All the experimental points of Fig. 2 are presented in this graph.

TABLE I. Typical parameters for the different materials studied. K is the director elastic coefficient, γ is the director viscosity coefficient, n_o is the ordinary refractive index, n_e is the extraordinary refractive index, τ_d is the characteristic director relaxation time, γ^* is the director diffusion coefficient, I_{Fr} is the threshold for the Fréedericksz transition, I_{SF} is the threshold for self-focusing, and n_2 is the Kerr nonlinear coefficient. K , γ , n_o , and n_e are taken from the data sheet provided by British Drug Houses [15]. The other parameters are from our measurements. τ_d , γ^* , and I_{Fr} are measured by the relaxation-rate technique described in the Appendix [see Eq. (A1)]. I_{SF} and n_2 are obtained from a linear fit of the focusing power as a function of the input intensity (see Sec. II).

Sample	K (10^{-7} dyn)	γ ($\text{g cm}^{-1} \text{s}^{-1}$)	n_o	n_e	τ_d (s)	γ^* ($10^{-6} \text{ cm}^2/\text{s}$)	I_{Fr} (kW/cm^2)	I_{SF} (kW/cm^2)	n_2 ($10^{-4} \text{ cm}^2/\text{kW}$)
MBBA	8	0.77	1.55	1.76					
MBBA 100 μm					18	1	1.12	1.6	2.5
MBBA 1000 μm					184				
6CB	7	0.37	1.53	1.7					
6CB 100 μm					6	2.7	0.87	1.25	0.87
6CB 700 μm					170				
6CB drop					95	10			
E209	8 to 20	0.35	1.51	1.68					
E209 100 μm					5	2	7.72	9.3	5.4
E209 1000 μm									
E209 tube					70	28			

normalization factor (d_e/d) takes into account the thickness dependence of n_2 , measured only in thin samples ($d_e=100 \mu\text{m}$). Note that there is no theoretical justification for this choice of R . At least, as shown in Fig. 3, it brings the data for each material onto a single curve. If each material presents the same qualitative shape, there is still a factor of 4 between the different liquid crystals. Our scaling has to include the material parameters in a more refined way than just n_2 , in order to bring all the different liquid crystals into one curve.

Let us note that a break in the curves appears consistently around $d/f \sim 1$, compatible with the previous analysis. Once the thin sample approximation breaks down, the focal point being inside the nematic liquid crystal, the best geometry to study is the semi-infinite sample. Increasing the thickness of flat samples does not help in this respect: for the thickest sample ($d=2000 \mu\text{m}$), the beam breaks into filaments, rendering our measurement-technique useless. We have to adopt a new geometry, described in the next section.

III. SELF-FOCUSING IN CYLINDRICAL GEOMETRY

We studied in the previous section the sample focal power, i.e., the effect of the beam on the nematic. We now explore the self-focusing of the beam itself in a cylindrical geometry. This configuration allows both visualization of the beam and local cooling around its axis. We show that the low-intensity behavior is consistent with the results of Sec. II.

A. Experimental setup

In order to prevent a possible transition to the isotropic phase at high intensity, we use the liquid crystal E209, which offers a much wider range in temperature

for the nematic phase (-50 to 111°C). A glass capillary of inner diameter 1.5 mm is coated with the polymer (3-amino-propyl trimethoxy-silane) (MAP) to ensure tangential alignment of the director at the surface [see Fig. 4(b)]. The liquid crystal in the nematic phase is then injected inside, the shear flow aligning the director parallel to the surface. The sample can be cooled down to a minimum temperature of -40°C , using a flow of nitrogen gas around the capillary. A heat exchanger is used to cool

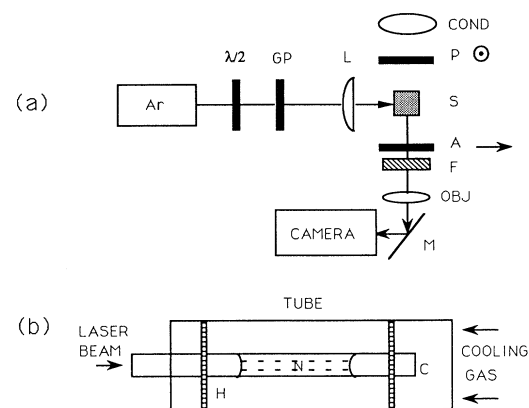


FIG. 4. (a) Observation setup for samples in cylindrical and spherical geometries: Ar, Argon laser; $\lambda/2$, half wave plate; GP, Glan polarizer; L, converging lens; S, sample (either a spherical drop inside a cuvette or a tube); COND, microscope condenser; P, sheet polarizer; A, analyzer; F, red color filter (used when looking at the director orientation); OBJ, microscope objective; M, mirror. (b) Details of the tube setup: The outside cylindrical tube is 1 cm in diameter and serves to cool the capillary C via flowing nitrogen gas; H are the supports for the capillary. The nematic sample N is aligned parallel to the capillary walls, forming a meniscus at the interface.

the gas. However, in most of our experiments we use a direct nitrogen flow at room temperature to evacuate the excess heat. The temperature rise of the sample is measured to be less than 10°C . One end of the capillary is sealed to avoid any motion of the liquid crystal. We verified that the sample does not show any sign of convection or transition to the isotropic phase up to 10 W in input power. Thus, within our range of intensities, we conclude that heating effects are unimportant.

In the experimental setup shown in Fig. 4, the tube filled with the liquid crystal in the nematic phase sits horizontally on the stage of an inverted microscope. The Argon laser beam is aligned along the tube axis and is linearly polarized. A precise alignment of the beam along the tube axis is crucial. The beam intensity (our control parameter) is adjusted by displacing a 50-mm converging lens placed before the sample, which controls the beam spot size. However, the strongest lens in our system is the front meniscus at the air-nematic interface [Fig. 4(b)], which makes the initial beam slightly diverging. We checked that the reported observations do not depend upon the nematic orientation caused by the meniscus. In fact, we recover the same phenomena with a spherical meniscus (see Sec. V), and also with a flat one. This last geometry was achieved by closing one end of the capillary with a flat coverslip, coated with silane to ensure homeotropic alignment of the director on its surface. The length of the nematic sample is typically 2 cm. By looking directly at the scattered light of the argon laser beam with the microscope, we observe self-focusing inside the nematic liquid crystal. Scattering losses limit the length of the nematic over which the light affects the director orientation. However, a lower limit to the scattering length was measured below the Fréedericksz threshold to be around 4 mm. In the focusing regime, this length increases up to 15 mm, due to the suppression of the thermal fluctuations of the director orientation by the electric field. Scattering losses are thus negligible on the length scale of the observed phenomena.

B. Low-intensity behavior

Let us turn to the transverse observation of the beam. Looking at Figs. 5(a) to 5(f), one distinguishes two distinct components of the beam: a diverging halo that does not evolve, and a bright central part, the focal point of which recedes towards the entrance meniscus as the intensity is increased. This is due to the birefringing nature of the nematic phase. The beam, as it crosses the air-nematic-phase interface, breaks into the ordinary and extraordinary components. The ordinary one, the diverging halo, experiences a constant refractive index medium and does not suffer any bending or focusing.

Let us now concentrate on the evolution of the extraordinary component of the beam. Measuring the distance from the entrance meniscus to the focal spot gives, up to an additive constant, the relation between f^{-1} , the equivalent focal length of the system, and the laser intensity (Fig. 6). Note that contrary to the case of plane samples, we do not measure the distance of the waist from the plane of the initial beam waist, because of the initial

divergence of the beam. It is thus impossible to get the absolute value of $1/f$.

Depending upon the initial diverging angle of the beam, the two regimes described before are observed: a linear increase of $1/f$ with the beam intensity in Fig. 6(a), and an exponential one in Fig. 6(b). The observed linear dependence is surprising when one realizes that the focal point is always inside the sample, and thus that we should observe the regime $d/f > 1$, as defined for flat samples. Because of a different positioning of the external lens with respect to the meniscus, the beam at low intensity is more diverging in Fig. 6(a) than in Fig. 6(b), and produces a smaller excited nematic region. Thus, while in Fig. 6(a) the focal point is always outside this active nematic region (corresponding to $d/f < 1$ in planar geometry), in Fig. 6(b) it recedes backwards into it (corresponding to $d/f \geq 1$ in planar geometry). The focusing effect is sharply enhanced in the latter case, which is compatible with what has been observed in plane samples. Thus this feature of self-focusing is robust and does not depend on the detailed geometry of the system. However, the beam intensity was the same in the two cases,

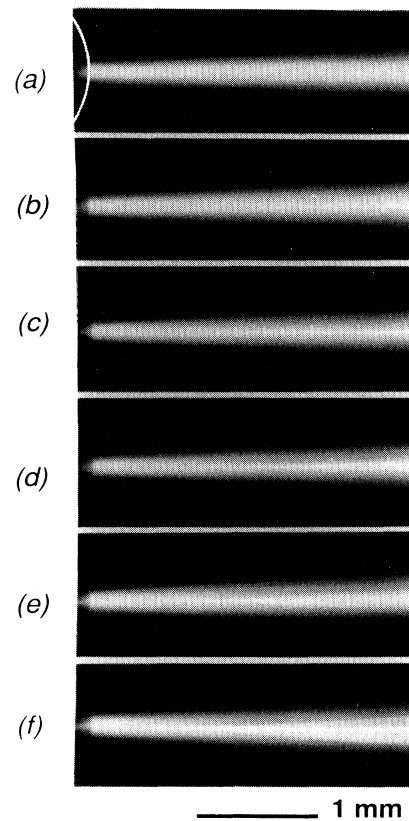


FIG. 5. Onset of self-focusing in a tube of E209; the beam is coming from the left. The white line in Fig. 5(a) represents the air-nematic-phase meniscus, which is at the same position for the following pictures. The tube diameter is 1.5 mm. The experiment is performed at room temperature, with a flow of Nitrogene around the capillary. The beam intensities are, respectively, (a) 0.15, (b) 0.63, (c) 0.71, (d) 0.74, (e) 0.80, and (f) 0.84, in kW/cm^2 .

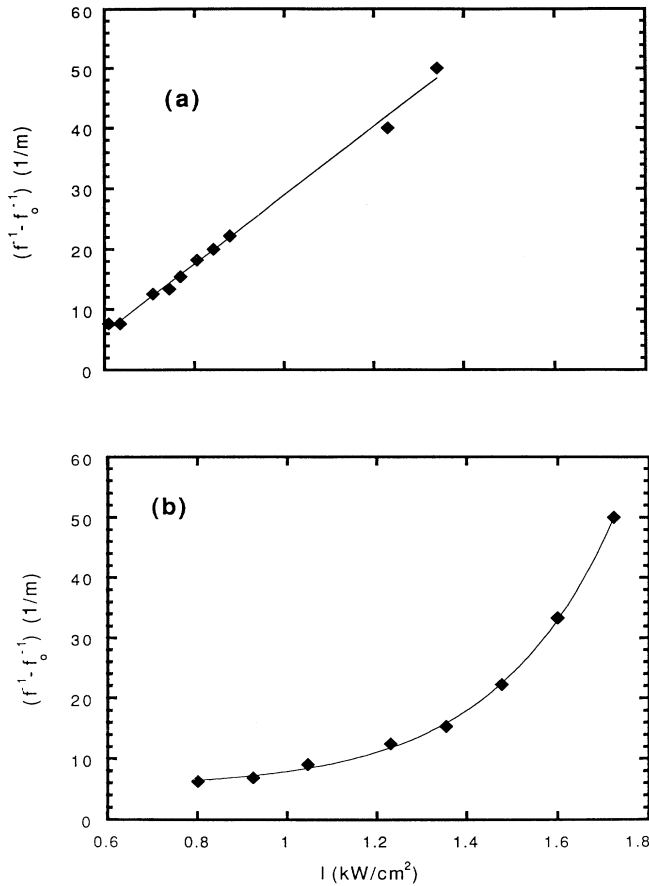


FIG. 6. Focal power for a tube of E209 vs intensity, for two different initial diverging angles of the laser beam. The beam at minimum intensity is more diverging in (a) than in (b). $1/f$ is known up to an additive constant $1/f_0$. The lines are best fits for the data: linear fit in (a), and exponential fit in (b).

indicating that it is not the correct control parameter. As in Sec. II (see the definition of R), the length of the active nematic region d has to be included.

A measurement of the exponential decrease of $1/f$ as a function of time, when rapidly switching the intensity down, allows the determination of the director diffusion coefficient which is reported in the table [$1/f$ is proportional to $n_2(I - I_{SF})$, i.e., the square of the director deformation angle]. Taking the tube diameter as the typical length, we extract the value for the director diffusion coefficient γ^* , as described in the Appendix. This value, reported in the table, is much higher than in the flat sample, because of the bigger elastic constraints in the cylindrical geometry.

If the low-intensity behavior is identical to the case of plane samples, the specific cylindrical geometry of the system affects self-focusing in an important way, as discussed in the next section.

IV. STRONG SELF-FOCUSING IN CYLINDRICAL GEOMETRY

We now explore the strong intensity regime in the cylindrical geometry. By increasing the input intensity we encounter first a local saturation of the focusing effect, then an undulation of the beam and the breaking of it into filaments. The experimental setup is the same as described in the previous section.

A. Saturation

The focal point recedes towards the meniscus when the input intensity increases, as explained before. This is shown in Figs. 7(a) and 7(b), the intensity ranging from $1.35 kW/cm^2$ to $1.57 kW/cm^2$. It then reaches a stable position close to the meniscus ($\sim 150 \mu m$), and does not move any more when the intensity is further increased, as shown in Figs. 7(c) to 7(f). We refer to this behavior as a

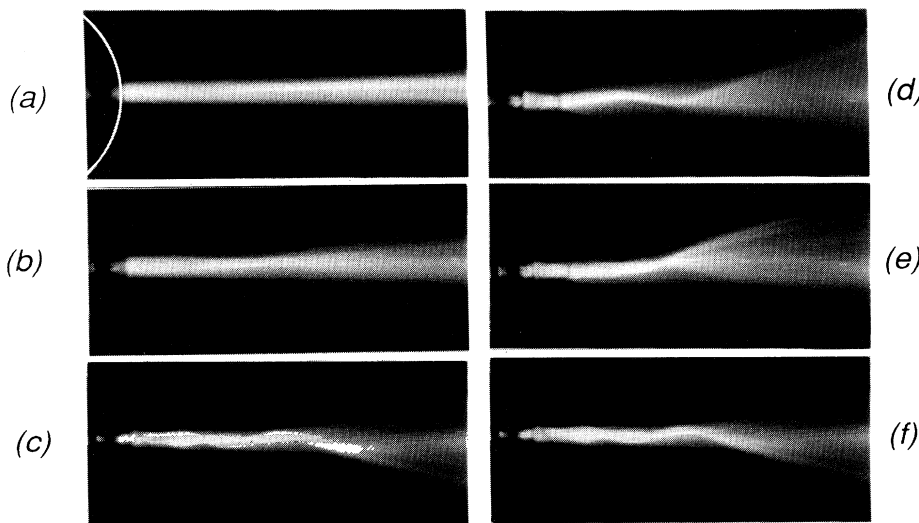


FIG. 7. Onset of beam undulation in a tube of E209; the beam is coming from the left. The white line in Fig. 5(a) represents the air-nematic-phase meniscus, at the same position for the following pictures. The tube diameter is 1.5 mm. The experiment is performed at room temperature, with a flow of Nitrogene around the capillary. The beam intensities are, respectively, (a) 1.35, (b) 1.57, (c) 1.78, (d) 1.87, (e) 1.98, and (f) 2.4, in kW/cm^2 .

1 mm

local saturation of self-focusing. It is only local because the focusing is still globally evolving in space: Figs. 7(d) to 7(f) show a beam undulation growing far from the meniscus. This undulation is the subject of the next paragraph. We also observe this local saturation in a spherical geometry, but not in a planar one; it is geometry dependent. Saturation occurs when the director keeps an almost fixed orientation, either because it is already parallel to the electric field, or because the elastic force is too important. We do not observe any saturation of the focusing power in plane samples because the weaker transverse elastic constraints in this case bring the observation window for local saturation out of our intensity range.

B. Undulation

Increasing the intensity above the saturation point leads to a dramatic change in the shape of the beam: it develops a transverse oscillatory mode, the characteristic length of which decreases with intensity. We see in Fig. 7(d) such an undulation at an intensity of 1.87 kW/cm^2 . Figures 7(e) and 7(f) show the decrease of the longitudinal wavelength of the undulation with intensity: compare Fig. 7(d) ($I = 1.87 \text{ kW/cm}^2$), where one observes only one undulation, to Fig. 7(f) ($I = 2.4 \text{ kW/cm}^2$), where three wavelengths are visible. The largest length scale observed was of the order of the tube diameter.

We now present a simple physical model to explain this beam undulation. In the experiment, the liquid crystal is a uniaxial birefringing medium; its optical axis is the director \mathbf{n} . Let us first recall the usual properties of uniaxial crystals [21]. Figure 8(a) shows a cross section of

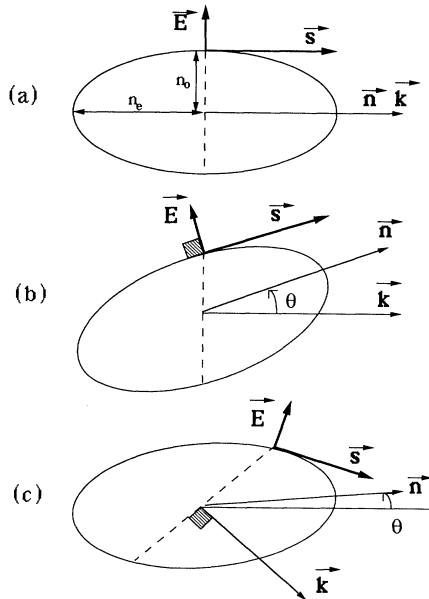


FIG. 8. Cross section of the ellipsoid of wave normals and the vector fields inside a tube of nematic liquid crystal. \mathbf{n} is the director, \mathbf{k} is the wave vector, \mathbf{E} is the electric field, \mathbf{s} is the Poynting vector, and θ is the deformation angle. The beam is (a) at the air–nematic-phase interface, (b) at the center of the sample, and (c) away from the center.

the so-called ellipsoid of wave normals, whose axis of rotation is the director \mathbf{n} . If \mathbf{k} is the wave vector, the intersection of the plane perpendicular to \mathbf{k} with this ellipsoid is an ellipse. The main principal axis is shown in Figs. 8(a) to 8(c) (dashed line). Its length is the optical index seen by the extraordinary ray. Only the extraordinary ray responds to a rotation of the optical axis with respect to \mathbf{k} . The ordinary ray, associated with the other principal axis (pointing out of the page), keeps a fixed direction inside the medium, and does not exhibit any focusing, bending, or splitting. The directions of the electric field \mathbf{E} and Poynting vector \mathbf{s} are constructed in the usual way. At the point where the principal semiaxis intersects the ellipsoid, \mathbf{E} is always perpendicular and \mathbf{s} tangent to the ellipsoid.

Let us now follow the beam inside the nematic. At the air–nematic-phase interface, the orientations of the vector fields are shown in Fig. 8(a). The wave vector \mathbf{k} is aligned with \mathbf{s} and \mathbf{n} , and \mathbf{E} is perpendicular to \mathbf{k} . The light is still a transverse wave.

Inside the medium, as \mathbf{n} tends to align along the direction of \mathbf{E} , the ellipsoid rotates, either up or down. Let us suppose a positive angle of rotation θ . From Snell's law, \mathbf{k} is fixed in space and perpendicular to the air–nematic-phase interface, which we suppose vertical. The direction of \mathbf{s} and \mathbf{E} will then change according to the rotation of the ellipsoid [Fig. 8(b)]. Since energy is transported along \mathbf{s} , the beam will bend in the \mathbf{s} direction, and moves up away from the center of the sample.

When the beam is away from the center, the vector fields are as shown in Fig. 8(c). Because of the boundary conditions which fix the director at the surface, the effect of the beam on the nematic phase gets smaller as one approaches the boundaries. The first effect is that θ is smaller than in Fig. 8(b). The second effect is that there is now a transverse gradient of optical index, pointing towards the center of the tube, because of the asymmetry in the elastic restoring torque at the beam position: the farther away from the boundary, the weaker the restoring torque, the bigger the angle θ for a same beam intensity, the bigger the refractive index n_e . As \mathbf{k} is bent towards the region of high optical index [down in Fig. 8(c)], \mathbf{s} follows it. The beam is attracted back to the center.

In conclusion, \mathbf{s} is first deflected away by the director reorientation and then pulled back by the index gradient imposed by the boundary conditions on the nematic phase. We experimentally verified that the undulation occurs in the plane defined by \mathbf{E} and \mathbf{n} , in agreement with the above simple picture. Even though the undulation results from a nonlocal, nonlinear interaction, the above heuristic picture captures the main physical mechanism, related to strong boundary effects.

C. Beam filamentation

For larger intensities ($I \sim 2 \text{ kW/cm}^2$), the beam develops an inner transverse structure composed of two distinct filaments undulating in phase opposition. Figures 10(a) to 10(d) show this effect for intensities ranging from 3 kW/cm^2 to 5 kW/cm^2 .

We measure the distance between the crossing points

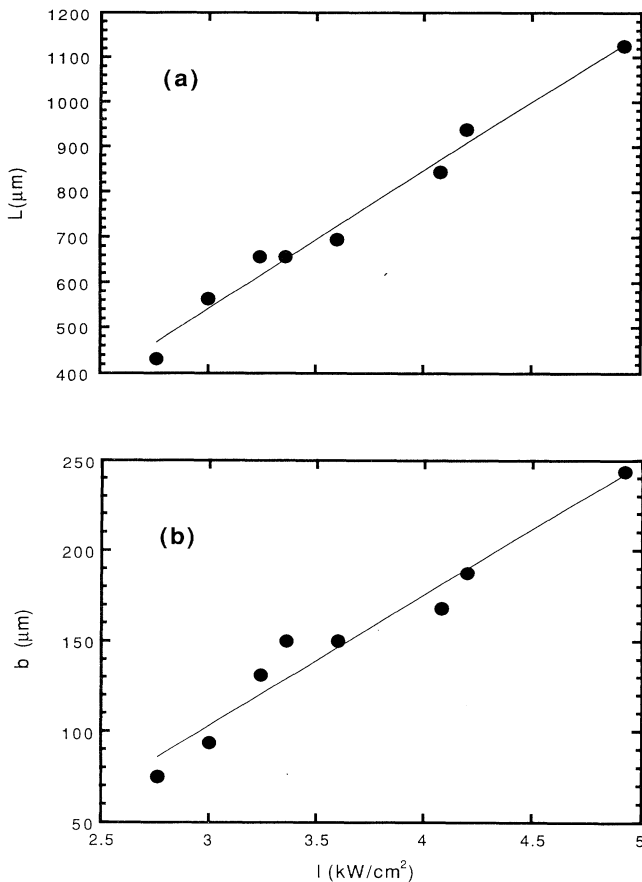


FIG. 9. In a tube of E209 (see Fig. 10), (a) the longitudinal distance between the crossing points of the two filaments vs the beam intensity, and (b) the transverse distance between the two filaments vs the beam intensity.

of the two filaments [Fig. 9(a)] and the maximum transverse separation between them [Fig. 9(b)] as a function of intensity. The first distance is characteristic of the longitudinal undulation of the beam, the second one of its transverse structure. As is shown in Figs. 9(a) and 9(b), both of these distances increase similarly with intensity. This is also seen in Figs. 10(a) to 10(d). The two orthogonal structures are connected. A striking point is the increase of the longitudinal beam undulation, as opposed to a decrease at lower intensity. This means that the spatial period of the beam undulation first decreases with intensity, reaches a minimum, then increases.

This surprising behavior is easily recovered in the heuristic picture described in the previous paragraph. As the intensity is increased close above the Fréedericksz threshold, the director reorientation brings the straight beam to undulate: the undulation wavelength decreases from infinity to a finite value. On the other hand, when the intensity is so high as to rotate the director by $\pi/2$ in Fig. 8(b), the ellipsoid construction indicates that the extraordinary beam propagates straight parallel to the beam axis (infinite undulation wavelength). A turnaround has then to take place between the two asymptotic regimes. A detailed mathematical analysis is consistent with this physical intuition [12].

The last two pictures [Figs. 10(e) and 10(f)] are taken at high intensity, 24 kW/cm^2 and 36 kW/cm^2 , respectively. The beam undulation is still observed. However, the two filaments are now oscillating in parallel around the beam axis [Fig. 10(e)]. At intensities higher than in Fig. 10(f), the beam exhibits a random dynamic behavior. We have thus reached the limit of steady self-focusing in nematic liquid crystals.

D. Multiple focal points

Another set of observations was performed at a lower temperature (-2°C). Again the beam developed an in-

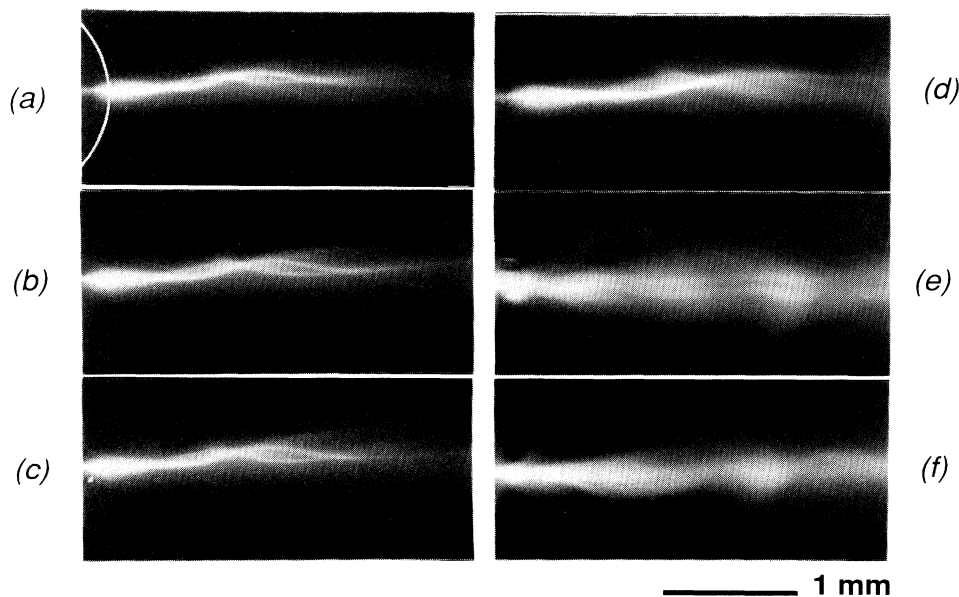


FIG. 10. High-intensity beam undulation in a tube of E209; the beam is coming from the left. The white line in Fig. 5(a) represents the air-nematic-phase meniscus, at the same position for the following pictures. The tube diameter is 1.5 mm. The experiment is performed at room temperature, with a flow of Nitrogene around the capillary. The beam intensities are, respectively, (a) 3, (b) 3.36, (c) 3.6, (d) 4.9, (e) 24, and (f) 36, in kW/cm^2 .

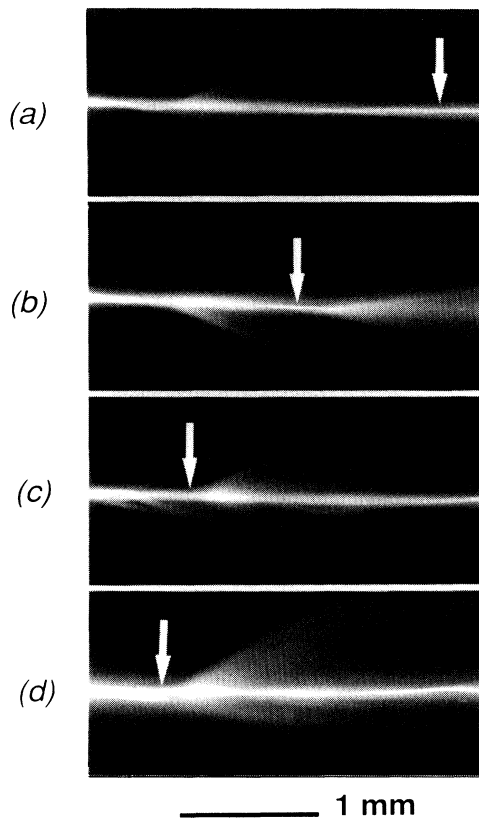


FIG. 11. Multiple focal points in a tube of E209; the beam is coming from the left. The temperature is $\sim 2^\circ\text{C}$. The white line in Fig. 5(a) represents the air–nematic-phase meniscus, at the same position for the following pictures. The tube diameter is 1.5 mm. The beam intensities are, respectively, (a) 21, (b) 24, (c) 26, and (d) 31, in kW/cm^2 .

interesting structure which at first glance was different from the ones described before. As before, a focal point recedes towards the entrance meniscus until local saturation is achieved. In this case, however, we observe (far from the meniscus) the appearance of a secondary focal point along the tube axis, as shown in Fig. 11(a). The arrow indicates the position of the focal point. It also recedes in turn, towards the first one as the intensity is increased [Figs. 11(a) to 11(d)]. In Fig. 11(d), a third focal point appears at the extreme right of the picture. Each of the secondary focal points recedes backwards and encounters a local saturation which causes it to stop at a fixed distance from the previous one. This saturation distance is found to be of the order of the oscillatory length scale previously described. One can see in Fig. 11(c) a small beam undulation close to the meniscus. These focal points could be what we previously described as crossing points, the optical resolution being too low to distinguish the filaments. Going to even lower temperatures did not bring any new observation.

V. SELF-FOCUSING IN SPHERICAL GEOMETRY

We describe in this section an observation of the beam in a spherical geometry. We suspend spherical drops of

nematic liquid crystal in a transparent gel (agarose). The gel structure compensates for the buoyancy force on the lighter liquid crystal and holds the drop in place. The strong surface tension ensures the spherical shape of the drop. While in the liquid phase, the gel is put into an optically flat glass cuvette. Drops of liquid crystal in the isotropic phase are then injected into the hot gel. We dope the gel with polyethylene glycol to induce a director tangent to the gel–nematic-phase interface. Upon cooling, two antipodal point defects called boojums [22,23] appear at the gel–nematic-phase interface and give a directionality to the drop. A typical drop is shown under crosspolarized illumination in Fig. 12. The visible boojum at the top of the drop is the point of convergence of the dark lines. The antipodal one is not in focus and hence does not appear in the picture.

The experimental setup is the same as in Fig. 4. The linearly polarized argon beam is aligned perpendicular to the line connecting the boojums, with its polarization perpendicular to it. The beam is focused from the side onto a drop of nematic liquid crystal, which sits inside a cuvette on an inverted microscope. We can either look at the scattered light of the beam or, placing a filter between the sample and the microscope objective, look at the drop using the microscope crosspolarized illumination. The laser beam spot size, at the entrance of the drop, is much smaller than the drop diameter d , and so experiences only a uniform orientation of the director. The gel–nematic-phase interface acts as the strongest converging lens in our system. The 50-mm lens before the sample is used to adjust the beam size, and thus the input intensity at the entrance to the drop.

At low intensity, a focal point appears inside the drop and moves backwards, until it reaches a stable position close to the entrance meniscus, as in the cylindrical case. Switching back the intensity to its minimum value, we record the exponential decay of the distance from the en-

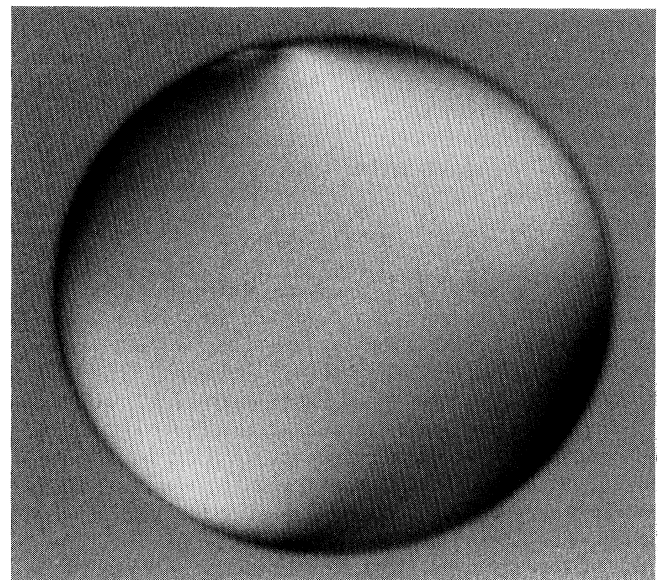


FIG. 12. Drop of 6CB (diameter $\sim 1450\ \mu\text{m}$) under crosspolarized illumination. Note the point defect at the top of the drop and the other one antipodal to it.

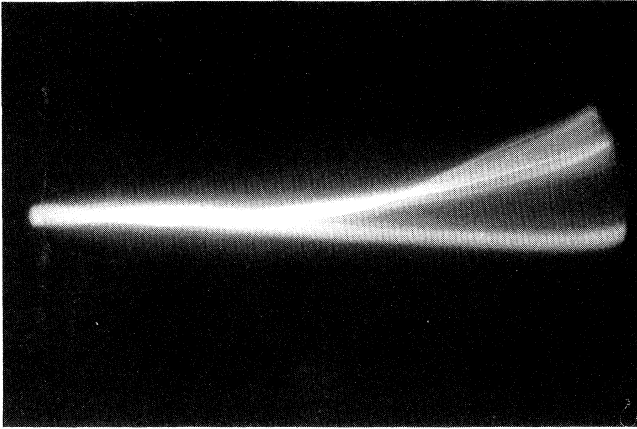


FIG. 13. Drop of E209, of diameter 2.8 mm. The two boojums are, respectively, at the top and bottom of the drop. The beam is coming from the left. The input intensity is ~ 5 kW/cm².

trance meniscus to the focal point with time. The characteristic director relaxation time τ_d is measured to be 95s for 6CB. The corresponding value of γ^* is 10^{-5} cm²/s, taking the diameter of the drop as a typical length. It is five times bigger than the value we found in planar samples because of the bigger elastic constraints in the spherical geometry.

At high intensity, we recover qualitatively the same phenomena reported in the previous section. Figure 13 shows a drop of E209, of diameter $d \sim 2.8$ mm, at an input intensity of 5 kW/cm². The two antipodal point defects are, respectively, at the top and bottom of the drop. The beam, coming from the left, splits into two components: the ordinary one that propagates straight, unaffected by the director orientation, and the extraordinary one, that exhibits undulation and filamentation. Up to four oscillations are observed in the figure. We thus believe that the simple picture using the ellipsoid of wave normals is appropriate to describe qualitatively the evolution of the beam inside the liquid crystal, and that the phenomena encountered (undulation, filamentation) are robust to the specific boundary conditions, as long as the director reorientation is constrained in the beam transverse direction.

VI. CONCLUSION

We have presented a detailed study of strong self-focusing of a laser beam in nematic liquid crystals in various geometries. Motivated by the sharp increase of the focal power as a function of the input intensity in planar geometry, and by the observed filamentation, we have visualized the phenomenon in a semi-infinite cylindrical configuration. The ability to evacuate the heat out, and the use of a liquid crystal with a wide temperature range for the nematic phase, enabled us to reach the limit of steady self-focusing in nematic liquid crystal.

If for thin samples in planar geometry only the phase of the wave front is modified as the beam crosses the liquid crystal, we clearly need to resort to a more elaborate nonlinear model, coupling the phase and the

amplitude of the light field to explain the exponential increase observed for thicker samples. The fact that this exponential increase appears also in long cylinders indicates that it is not sensitive to the exact geometry and boundary conditions of the system. It is certainly not due to heating effects (which reduce the nonlinearity [9,24–26] and are unimportant in the tube). We showed that the two distinct focusing behaviors for thin and thick samples can be encompassed in the same curve, but have not found a universal scaling for self-focusing in nematic liquid crystals.

In semi-infinite samples, in a cylindrical and spherical geometry, we observe a beam undulation and a filamentary structure. We report in cylindrical and spherical geometries the existence of a local saturation for the focusing of the beam. Using such a saturation effect, the existence of multiple focal points [27] has been predicted for self-focusing in an isotropic medium. Furthermore, a standard analysis within the framework of the nonlinear Schrödinger equation (NLS) also predicts a breaking of the beam into filaments [28–33].

We do in fact observe multiple focal points and a breaking of the beam into filaments. However, we do not think that these models apply to our experiment and we would like to emphasize, once again, the unusual optical effects of nematic liquid crystals.

As a matter of fact, the treatment of self-focusing within the NLS framework leads to the conservation of the beam momentum [31–35], which is not consistent with our observation of an undulation in the cylindrical geometry. However, a full treatment of the nematic-light interaction leads to a nonlocal partial differential equation, the analysis of which shows the possibility of momentum transfer between the beam and the liquid crystal, and the existence of an oscillatory solution. Note that, in this analysis, this undulation is due to the existence of uniform boundary conditions at a finite distance of the beam, and the model does not require any saturation of the focusing. The physical model we gave in Sec. IV captures both the birefringing effect and this boundary condition's restoring effect. It explains the beam undulation and describes qualitatively the dependence of the spatial undulation wavelength as a function of the input beam intensity. More important, the mathematical model clearly shows the separation of the focusing into two distinct problems: the outer one for the beam undulation, and the inner one for the beam structure. All these predictions are consistent with our observations. Details of this analysis are given elsewhere [12].

ACKNOWLEDGMENTS

It is a pleasure to thank David McLaughlin, David Muraki, and Michael Shelley for intensive discussions. We thank Gordon Cates and his group for generously letting us use their facilities.

APPENDIX

We present in this appendix measurements of the material parameters near the onset of the Fréedericksz transition in a planar geometry. We use the 100- μ m plane

samples, with the setup described in Fig. 1.

Any deformation of the nematic director inside the sample will affect the polarization of the transmitted probe beam. We measure this change in polarization using an analyzer, crossed with the initial polarization of the probe beam [36].

We first measure the threshold intensity I_{Fr} of the Fréedericksz transition, the onset of which is characterized by the divergence of the transition time scale. The experimental procedure is the following. We quickly increase the pump intensity from zero to a value well above threshold. The exponential increase in time of the transmitted probe intensity is recorded with a charge-coupled-device camera, defining a characteristic time for the director deformation τ_i as a function of the final pump intensity. Since the transmitted intensity is proportional to the square of the deformation angle (the order parameter of the transition) [34], the actual deformation time is twice the measured one. It can be written as [37]

$$\tau_i = (d/\pi)^2 (\gamma^*)^{-1} I_{Fr} / (I - I_{Fr}), \quad (\text{A1})$$

where I is the pump intensity, d is the thickness of the sample, $\gamma^* = K/\gamma$ is the director diffusion coefficient, K is the elastic constant, and γ is the viscosity coefficient for the director. From a linear fit of the values of $(1/\tau_i)$ versus the pump intensity, we deduce I_{Fr} and γ^* . These values are reported in the table. Note that the reported

values of γ^* are in good agreement with the ones estimated from the values of K and γ given in the table ($\gamma^* = K/\gamma$).

We also measure the characteristic director relaxation time. Switching off the beam intensity from a given value above threshold, we record the exponential decrease with time of the transmitted probe intensity and measure the characteristic relaxation time τ_d . It can be written as [37] $\tau_d = (d/\pi)^2 (\gamma^*)^{-1}$. The values of γ^* estimated from these measurements are found to be in good agreement with the ones obtained from Eq. (A1).

We can also associate a characteristic length to the transition. The Fréedericksz coherence length for the director deformation ξ is similar to the one defined for a uniform dc field [16]:

$$\xi^2 = (K/\Delta\epsilon)(c/n_o)I^{-1}, \quad (\text{A2})$$

where $\Delta\epsilon$ is the (optical) dielectric anisotropy, c is the speed of light, and n_o is the ordinary optical index. From known values of the parameters K and $\Delta\epsilon$, we can estimate ξ . We find for 6CB and MBBA, $\xi \sim 25 \mu\text{m}(I)^{-1/2}$ and for E209, $\xi \sim 40 \mu\text{m}(I)^{-1/2}$, where I is in kW/cm^2 . From these values, the onset of the Fréedericksz transition is estimated assuming a sinusoidal mode near onset: $\xi \sim (d/\pi)$. Using the material parameters, we get $I_{Fr} \sim 0.7 \text{ kW}/\text{cm}^2$ for 6CB and MBBA and $I_{Fr} \sim 2 \text{ kW}/\text{cm}^2$ for E209, in reasonable agreement with the values reported in the table.

*Also at NEC Research Institute, 4 Independence Way, Princeton, NJ 08540.

- [1] R. Y. Chiao, E. Garmire, and C. H. Townes, *Phys. Rev. Lett.* **13**, 479 (1964).
- [2] P. L. Kelley, *Phys. Rev. Lett.* **15**, 1005 (1965).
- [3] S. A. Akhmanov, A. P. Sukhorukov, and R. V. Khokhlov, *Usp. Phys. Nauk* **10**, 19 (1968) [*Sov. Phys. Usp.* **93**, 609 (1968)].
- [4] S. A. Akhmanov, R. V. Khokhlov, and A. P. Sukhorukov, in *Laser Handbook*, edited by F. T. Arecchi (North-Holland, Amsterdam, 1972).
- [5] O. Svelto, in *Progress in Optics XII*, edited by E. Wolf (North-Holland, Amsterdam, 1974).
- [6] Y. R. Shen and J. H. Marburger, *Prog. Quantum Electron.* **4**, 1 (1975).
- [7] Y. R. Shen, *The Principles of Nonlinear Optics* (Wiley, New York, 1984).
- [8] *Instabilities and Chaos in Quantum Optics*, edited by F. T. Arecchi and R. G. Harrison (Springer-Verlag, Berlin, 1987).
- [9] I. C. Khoo and Y. R. Shen, *Opt. Eng.* **24**, 579 (1985).
- [10] N. V. Tabiryan, A. V. Sukhov, and B. Y. A. Zel'dovich, *Mol. Cryst. Liq. Cryst.* **136**, 1 (1986).
- [11] I. C. Khoo, in *Progress in Optics XXVI*, edited by E. Wolf (Elsevier, New York, 1988), p. 108.
- [12] E. Braun, L. P. Faucheux, A. Libchaber, D. W. McLaughlin, D. Muraki, and M. Shelley (unpublished).
- [13] All liquid crystals are purchased from British Drug Houses (BDH Limited, Broom Road, Poole, BH124NN, England).
- [14] Torr Seal is a low-vapor-pressure resin purchased from Varian Associates, Vacuum Products Division, Lexington, MA.
- [15] ZLI-3124 purchased from EM Industries, Inc., 5 Skyline Drive, Hawthorne, NY 10532.
- [16] P. G. de Gennes, *The Physics of Liquid Crystals* (Clarendon, Oxford, 1974).
- [17] P. P. Banerjee, R. M. Misra, and M. Maghraoui, *J. Opt. Soc. Am. B* **8**, 1072 (1991).
- [18] I. C. Khoo, S. L. Zhuang, and S. Shepard, *Appl. Phys. Lett.* **39**, 937 (1981).
- [19] B. Ya. Zel'dovich, N. F. Pilipetskii, A. V. Sukhov, and N. V. Tabiryan, *Pis'ma Zh. Eksp. Teor. Fiz.* **31**, 287 (1980) [*JETP Lett.* **31**, 263 (1980)].
- [20] N. F. Pilipetskii, A. V. Sukhov, N. V. Tabiryan, and B. Ya. Zel'dovich, *Opt. Commun.* **37**, 280 (1981).
- [21] M. Born and E. Wolf, *Principles of Optics* (Pergamon, New York, 1970).
- [22] G. E. Volovik and O. D. Lavrentovich, *Zh. Eksp. Teor. Fiz.* **85**, 1997 (1983) [*Sov. Phys. JETP* **58**, 1159 (1983)].
- [23] M. V. Kurik and O. D. Lavrentovich, *Usp. Fiz. Nauk* **154**, 381 (1988) [*Sov. Phys. Usp.* **31**, 196 (1988)].
- [24] D. J. Kinzer and G. M. Morris, *Appl. Opt.* **25**, 1335 (1986).
- [25] H. Hsiung, L. P. Shi, and Y. R. Shen, *Phys. Rev. A* **30**, 1453 (1984).
- [26] I. C. Khoo and R. Normandin, *IEEE J. Quantum Electron.* **QE-21**, 329 (1985).
- [27] W. G. Wagner, H. A. Haus, and J. H. Marburger, *Phys. Rev.* **175**, 256 (1968).
- [28] V. I. Bespalov and V. I. Talanov, *Pis'ma Zh. Eksp. Teor. Fiz.* **3**, 471 (1966) [*JETP Lett.* **3**, 307 (1966)].

- [29] J. H. Marburger and E. Dawes, *Phys. Rev. Lett.* **21**, 556 (1968).
- [30] M. D. Feit and J. A. Fleck, Jr., *J. Opt. Soc. Am. B* **5**, 633 (1988).
- [31] A. J. Campillo, S. L. Shapiro, and B. R. Suydam, *Appl. Phys. Lett.* **23**, 628 (1973).
- [32] A. J. Campillo, S. L. Shapiro, and B. R. Suydam, *Appl. Phys. Lett.* **24**, 178 (1974).
- [33] S. Dyachenko, A. C. Newell, A. Pushkarev, and V. E. Zakharov, *Physica D* **57**, 96 (1992).
- [34] G. A. Schwartzlander, Jr., H. Yin, and A. E. Kaplan, *J. Opt. Soc. Am. B* **6**, 1318 (1989).
- [35] G. A. Schwartzlander, Jr. and A. E. Kaplan, *J. Opt. Soc. Am. B* **5**, 765 (1988).
- [36] G. K. L. Wong and Y. R. Shen, *Phys. Rev. A* **10**, 1277 (1974).
- [37] S. D. Durbin, S. M. Arakelain, and Y. R. Shen, *Phys. Rev. Lett.* **47**, 1411 (1981).

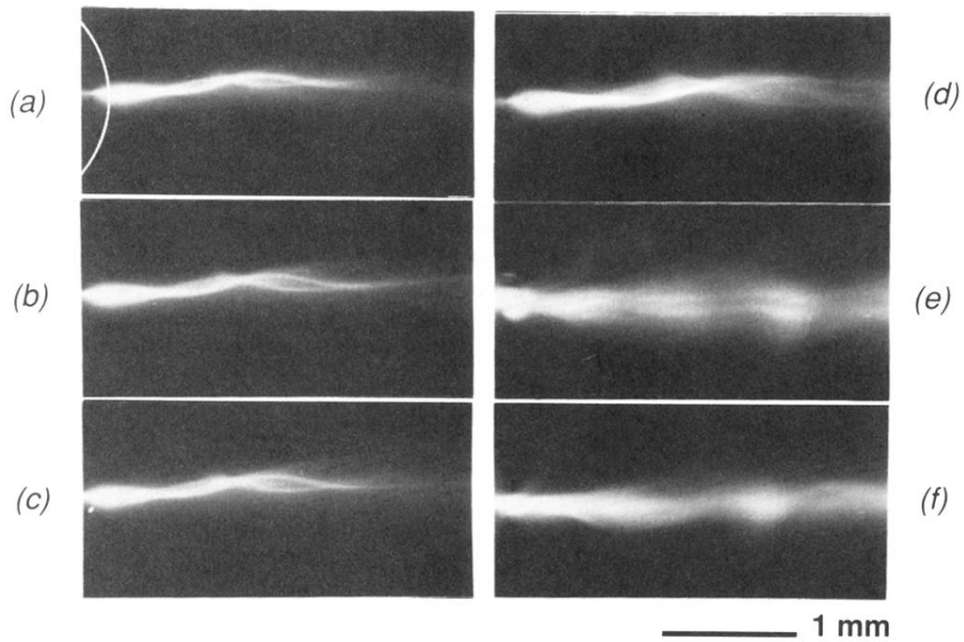


FIG. 10. High-intensity beam undulation in a tube of E209; the beam is coming from the left. The white line in Fig. 5(a) represents the air-nematic-phase meniscus, at the same position for the following pictures. The tube diameter is 1.5 mm. The experiment is performed at room temperature, with a flow of Nitrogene around the capillary. The beam intensities are, respectively, (a) 3, (b) 3.36, (c) 3.6, (d) 4.9, (e) 24, and (f) 36, in kW/cm^2 .

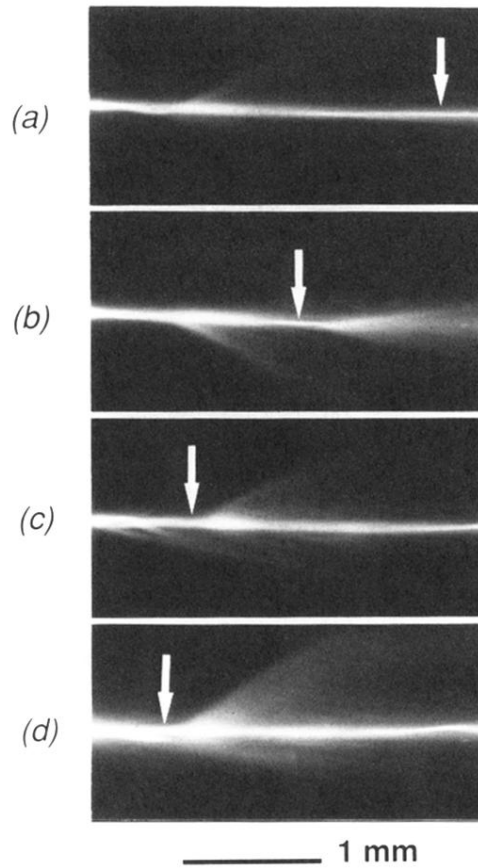


FIG. 11. Multiple focal points in a tube of E209; the beam is coming from the left. The temperature is $\sim 2^\circ\text{C}$. The white line in Fig. 5(a) represents the air–nematic-phase meniscus, at the same position for the following pictures. The tube diameter is 1.5 mm. The beam intensities are, respectively, (a) 21, (b) 24, (c) 26, and (d) 31, in kW/cm^2 .

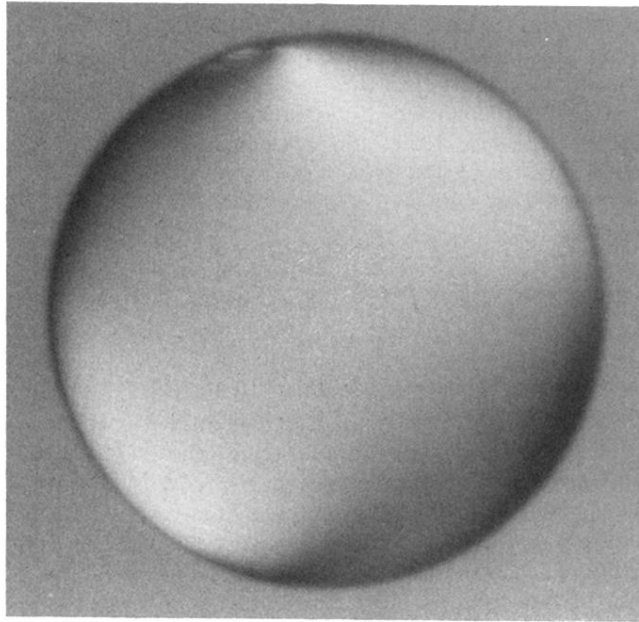


FIG. 12. Drop of 6CB (diameter $\sim 1450 \mu\text{m}$) under crosspolarized illumination. Note the point defect at the top of the drop and the other one antipodal to it.

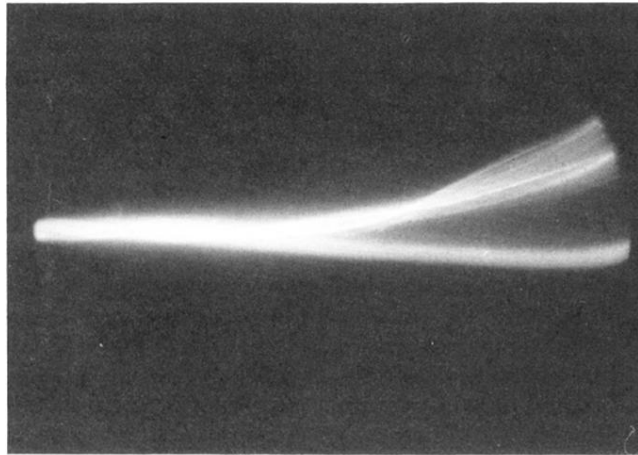


FIG. 13. Drop of E209, of diameter 2.8 mm. The two boojums are, respectively, at the top and bottom of the drop. The beam is coming from the left. The input intensity is ~ 5 kW/cm².

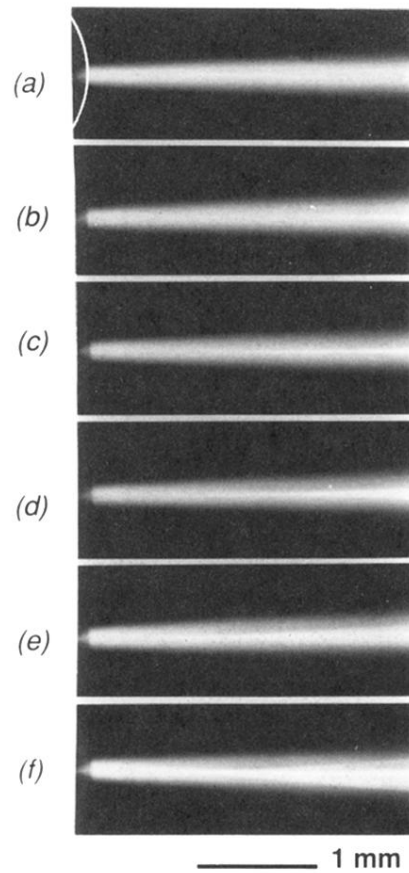


FIG. 5. Onset of self-focusing in a tube of E209; the beam is coming from the left. The white line in Fig. 5(a) represents the air-nematic-phase meniscus, which is at the same position for the following pictures. The tube diameter is 1.5 mm. The experiment is performed at room temperature, with a flow of Nitrogene around the capillary. The beam intensities are, respectively, (a) 0.15, (b) 0.63, (c) 0.71, (d) 0.74, (e) 0.80, and (f) 0.84, in kW/cm^2 .

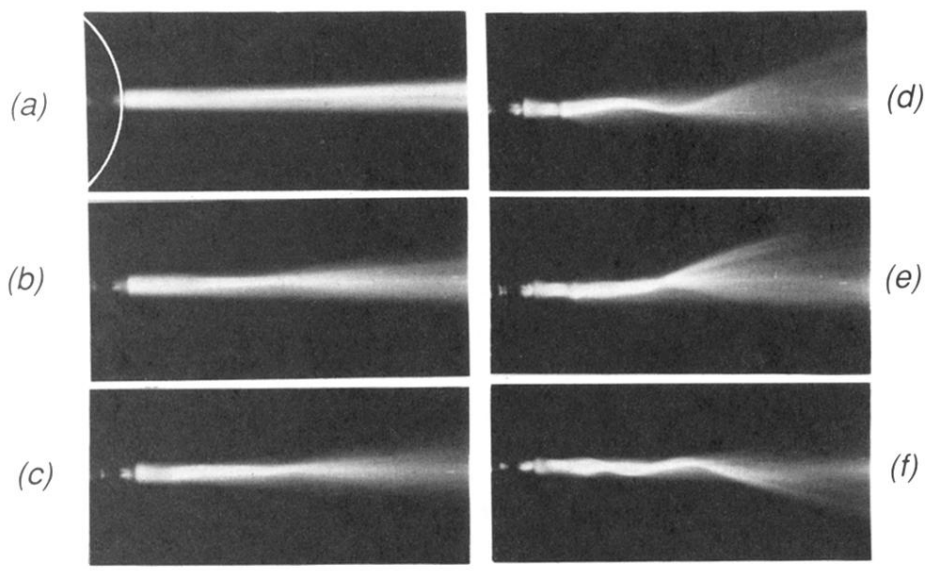


FIG. 7. Onset of beam undulation in a tube of E209; the beam is coming from the left. The white line in Fig. 5(a) represents the air-nematic-phase meniscus, at the same position for the following pictures. The tube diameter is 1.5 mm. The experiment is performed at room temperature, with a flow of Nitrogene around the capillary. The beam intensities are, respectively, (a) 1.35, (b) 1.57, (c) 1.78, (d) 1.87, (e) 1.98, and (f) 2.4, in kW/cm^2 .